An Optical Engine Used as a Physical Model for Studies of the Combustion Process Applying a Two-Color Pyrometry Technique

Lis Corral-Gómez [1] , **Octavio Armas** [1,*] , **José A. Soriano** [1] , **José V. Pastor** [2] , **José M. García-Oliver** [2] **and Carlos Micó** [2]

1. Universidad de Castilla-La Mancha, Campus de Excelencia Internacional en Energía y Medioambiente, Instituto de Investigación Aplicada a la Industria Aeronáutica, Escuela de Ingeniería Industrial y Aeroespacial, Av. Carlos III, s/n, 45071 Toledo, Spain; lis.corral@uclm.es (L.C.-G.); joseantonio.soriano@uclm.es (J.A.S.)
2. Universitat Politècnica de València, CMT-Motores Térmicos, Camino de Vera, s/n, 46022 Valencia, Spain; jpastor@mot.upv.es (J.V.P.); jgarciao@mot.upv.es (J.M.G.-O.); carmirec@mot.upv.es (C.M.)
* Correspondence: octavio.armas@uclm.es

Abstract: This work describes an experimental installation for the investigation of the combustion and injection processes. This installation is based on a two-stroke direct injection diesel engine with a total displacement of 3 L and a cylinder head equipped with three quartz windows. The windows are optical accesses that allow studying the process of injection, the atomization and evaporation of the fuel jet in an inert atmosphere (nitrogen), and the combustion process in a reactive atmosphere (ambient air). Additionally, the application of a two-color pyrometry technique to measure soot formation in this facility is presented. A methodological study is carried out regarding the influence of the dynamic range of the detectors and the wavelengths used. Maps of KL_{2C}, flame temperature, and error probability are presented. The use of cameras with high dynamic range provides better results since the system seems to be less sensitive to measurement noise, and fewer points are obtained with a non-physical solution. Moreover, an appropriate combination of interference filters can improve the reliability of the solution. The greater the difference between the wavelengths of both interference filters, the fewer points with a non-physical solution, which improves the reliability of results.

Keywords: optical engine; two-color pyrometry; combustion; injection processes; KL_{2C} maps; soot formation

1. Introduction

In the last few decades, the effects of engine exhaust emissions on the environment and the foreseen shortage of fossil fuels have been two very important challenges faced by society related to the use of internal combustion engines (ICEs). Society's development has been closely associated with the use of oil-derived fuels as a source of energy since its discovery and introduction at the end of the 19th century. Since then, worldwide oil consumption has increased and its applications have spread to many different aspects of our daily lives. Energy consumption is expected to increase by 56% between 2010 and 2040, with fossil fuels (which comprise coal, liquid, and gas fuels) playing an important role and accounting for almost 80% of global energy consumed [1–3].

On the other hand, unmanned aerial vehicles (UAVs) are increasingly used for military and civilian tasks. Power and endurance are two of the most important requirements to consider when choosing a UAV engine. Compared to electric motors, a reciprocating internal combustion engine (ICE) is a more favorable choice for use in some UAVs with large engines. In this work, a two-stroke diesel engine was used because the advantages of this type of engine, compared to other options, make its use possible in a non-negligible number of applications. Among the most notable advantages are its high efficiency, low cost,

simplicity, power, and high availability. It is a very well known and understood technology, and two-stroke engines tend to be air-cooled and, therefore, relatively lightweight and simple to integrate into vehicles. Among the applications for this type of engine, we find some types of UAVs [4,5]. An electric motor needs an auxiliary battery, and the energy density of batteries is lower than that of fuel. In addition, UAVs operate at low temperatures and high altitudes, and ICEs are best suited for these extreme conditions [6–13].

ICEs use liquid hydrocarbons as fuel to power them [10–12,14–16]. The burning of these fuels generates pollutant emissions that contain substances harmful to both the environment and human health [17–22]. Nitrogen oxide (NO_x) and particulate matter (PM) emissions, with soot as the main component, are regulated by emissions legislation [23,24]. Furthermore, soot formation can also influence engine performance and have feedback effects on the combustion and emission formation processes within the cylinder. Examples include heat losses from soot radiation heat transfer to engine walls [25,26] and NO_x formation from drops in flame temperature due to soot radiation heat transfer [27–29].

Therefore, a detailed investigation is required that allows a correct understanding of the phenomena that dominate the combustion process inside the cylinder and, consequently, the formation of the different pollutant species, so that solutions can be found to reduce emissions. To determine these parameters, experimental setups with optical accesses are used to allow studying the combustion process inside the combustion chamber [30]. Several experimental setups can be used as high-temperature, high-pressure vessels (HTHPs) [31–36] and optically accessible engines [37–40]. These experimental setups allow researchers to reproduce thermodynamic conditions, such as those present inside the cylinder of a reciprocating IC engine [37,41]. The optical accesses of experimental setups allow researchers to visualize the combustion process through the application of optical techniques [42].

The studies carried out to determine soot and flame temperatures in experimental setups by applying optical techniques include one carried out by Xuan T. et al. [30] that measured instantaneous soot production under low-soot conditions using a diffused back-illumination extinction technique (DBI) and two-color pyrometry simultaneously. This kind of study allows investigators to compare the performance of different techniques for measuring soot. From such studies, it can be concluded that despite certain uncertainties under high soot conditions, the two-color pyrometry technique offers the advantages of high time and spatial resolution, as well as the possibility of developing maps of soot concentration and flame temperature, unlike other methods [43–46]. Moreover, of the techniques mentioned above, only two-color pyrometry can be applied using only one optical access. For this reason, the technique has been chosen for use in many different works. Pastor J.V. et al. [47] used two-color pyrometry to analyze soot production in an optical engine with a Bowditch design and a real geometry quartz bowl [48] or a cylindrical-shaped bowl piston [47]. Zhang et al. [49] measured soot temperature and KL factor in a constant-volume chamber using the two-color pyrometry technique. Jeon J. and Park S. [50] studied the soot formation and oxidation processes in an optical CI engine using the two-color pyrometry technique. More complex optical setups can be found in the literature; such setups use three channels instead of two to improve sensitivity and accuracy in a wider range of temperatures [51].

Considering all of the above-mentioned facts, there is great interest in facilities with optical accesses that reproduce ICE operating conditions, as well as in the use of optical techniques to characterize combustion processes and pollutant formation. Therefore, the objectives of this article are twofold. First, we present an experimental setup based on a single-cylinder optical engine, which fills an existing gap between advanced, well-controlled test rigs and more conventional optical engines (i.e., those with a Bowditch-type optical access). This setup provides boundary conditions more similar to those of conventional engines than advanced testing rigs while remaining simpler than conventional optical engines. The second objective is to present a methodological study of two-color pyrometry to determine the effect of different experimental setup parameters on the results

obtained. The aim is to provide a detailed description of the facility, allowing the reproduction of ICE operating conditions and providing some guidelines to improve the accuracy of two-color pyrometry in future studies. The novelty of this work is that it presents an experimental facility and that the results of our study allow making a series of recommendations related to the optical setup of the two-color pyrometry technique. The rest of the work is organized as follows: (i) in Section 2, the experimental setup is described; (ii) in Section 3, the procedure employed in the study is explained; (iii) in Section 4, the results obtained are shown and discussed; (iv) in Section 5, the conclusions of the work are presented.

2. Experimental Facility Description

The experimental facility is composed of a reciprocating IC engine coupled to a drive system with an electric motor. This installation adds various independent auxiliary systems, such as: (i) a gas charging and transfer system in closed and open circuit, (ii) a common rail injection system, (iii) a lubrication and cooling system, (iv) a visualization system, and (v) a system for the control and data acquisition of engine parameters.

2.1. Gas Charging and Transfer System in Closed and Open Circuit

The experimental facility presented in this work allows the reproduction of thermodynamic conditions similar to those present within the cylinder of an actual reciprocating IC engine. Table 1 shows the operating condition ranges.

Table 1. Ranges of the operating conditions.

Parameter	Ranges	Units
In-cylinder gas pressure	4.5–8	MPa
In-cylinder gas temperature	800–900	K
In-cylinder gas density	17.7–35.3	kg/m^3

The experimental facility is designed to study the fuel spray injection, atomization, and evaporation processes under both inert and reactive atmospheres.

Inert Atmosphere and Closed Circuit

Figure 1 shows a scheme of the main gas circuit under an inert atmosphere configuration. It allows investigators to study the fuel spray under a non-oxidizing atmosphere. Pure nitrogen is used to fill the gas charging and transfer system in closed circuit; its thermophysical properties are like those of air. This configuration allows a complete visualization of the fuel spray evolution within the in-cylinder engine chamber without combustion.

Reactive Atmosphere and Open Circuit

In this case, as Figure 2 shows, fresh air flows through the circuit to supply the combustion chamber of the engine. It allows investigators to study the fuel spray under an oxidizing atmosphere.

The difference between the two circuits is that nitrogen circulates through the circuit in Figure 1, and fresh air circulates through the circuit in Figure 2.
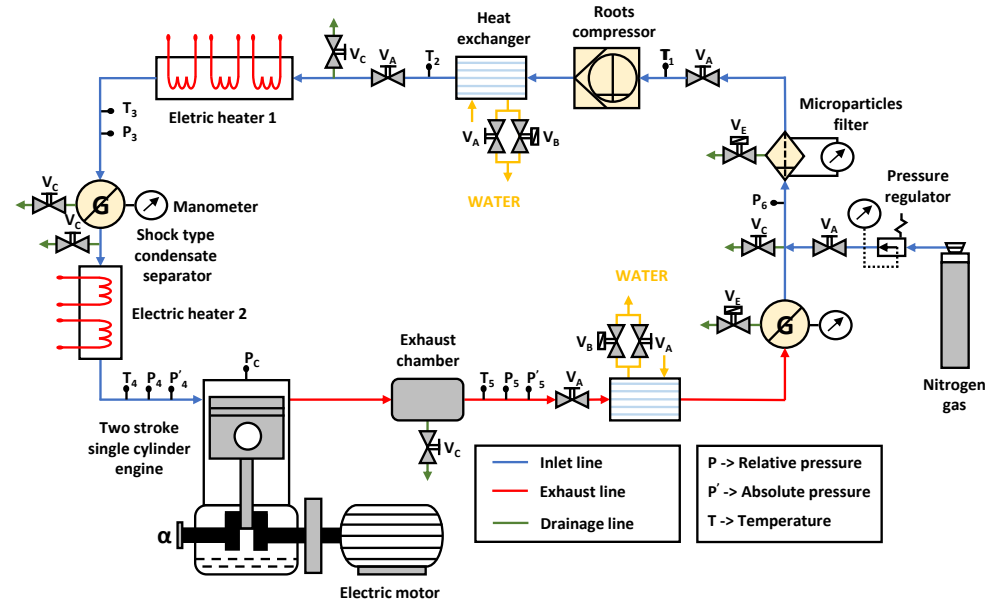
Figure 1. Scheme of the main gas circuit under an inert atmosphere configuration.
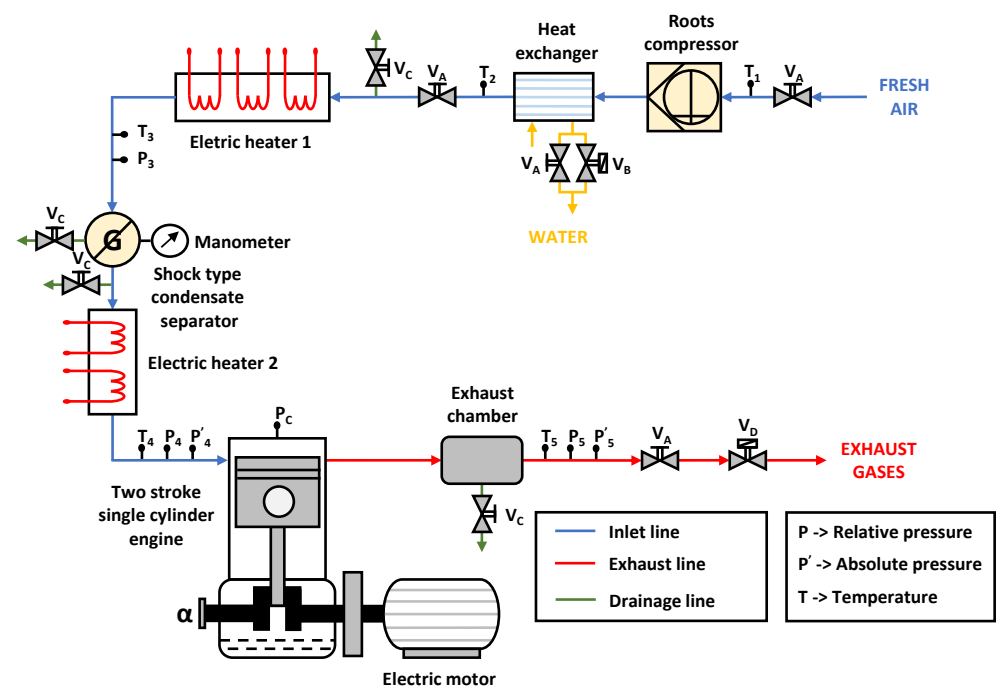

Figure 2. Scheme of the main gas circuit under a reactive atmosphere configuration.

2.2. Engine and Drive System

The main part of the experimental facility is an adapted version of a Jenbach JW-50 two-stroke, single-cylinder diesel engine with 3 L displacement. The main constructive characteristics of this engine are the following: cylinder diameter of 150 mm; total stroke of 170 mm; effective stroke of 108 mm, total original compression ratio of 26.3/1, original compression ratio of 17.1/1, and maximum rotational speed of 700 min^{-1}. The gas motion is produced through the inlet and exhaust ports, following a Curtis-type scavenging process. After the engine head modification, the effective compression ratio is around 9.5/1. In addition, the engine torque and power depend on the boost pressure and quantity of fuel injected, taking into account that the maximum in-cylinder pressure must be lower than 100 bar (10 MPa) to avoid the breakage of the quartz windows.

Figure 3 shows the cylinder head used. Four of the accesses are on the sides, and the other is on the top. The in-cylinder pressure sensor is mounted in one of the lateral accesses, while quartz windows (L88 × W37 × E28, R18 mm) are installed in the other three accesses. The quartz windows support a maximum pressure of 120 bar (12 MPa) and a maximum temperature of 1350 K. The upper access (D24 × L10.5 mm) is used to allocate the fuel injector.
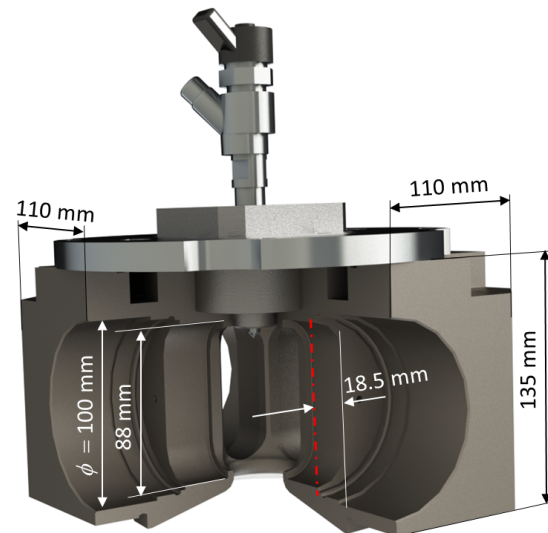
Figure 3. Modified engine head with selected dimensions.

Under the reactive atmosphere configuration, the fuel is injected once every 12–40 thermodynamic cycles. During each injection event, the amount of fuel injected (14–18 mg/stroke) was low enough in comparison to the amount of air inside the combustion chamber to not affect the in-cylinder thermodynamic conditions until the start of combustion. Moreover, it also ensured minimal window fouling.

2.3. Fuel Injection System

The injection system allows the injection event to be carried out inside the combustion chamber. Figure 4 shows a scheme of the injection system. The system is equipped with a Bosch common-rail system with a capacity of 20 cm^3 that allows it to reach injection pressures up to 1300 bar (13 MPa). The fuel injector is configured with a single-hole axial nozzle with a K factor of 1.5 and a hole diameter of 0.140 mm.

2.4. Visualization System

The visualization system used in the experimental facility for the study of combustion is the two-color pyrometry system. Figure 5 shows a typical schematic diagram of the two-color pyrometry system, which was used in the experimental facility of this work.

The two-color pyrometry system consists of two high-speed cameras, namely the Fastcam Photron SA-5 and the Photron SA-X2 with a Carl Zeiss Makro-Planar T* 2/100 lens. One of them is located looking directly into the combustion chamber, and the other is located in a perpendicular position. The light from the flame reaches the beam splitter, oriented at 45 degrees with respect to both cameras. The beam splitter transmits 50% of the light and reflects the other 50%, allowing the simultaneous visualization of flame radiation with the two detectors. An interference filter with a transmission band centered at 650 nm (red), 550 nm (green), or 450 nm (blue) and 10 nm FWHM is placed in front of each camera lens of each camera to ensure that only the desired wavelength is registered while the rest of the light is rejected. In addition, a neutral density filter (10, 30, 50, or 70% transmission) is included in front of each camera to regulate the light intensity received. The reason for

using these elements is that they enable the setting of similar acquisition parameters in both cameras while avoiding saturating either of them.
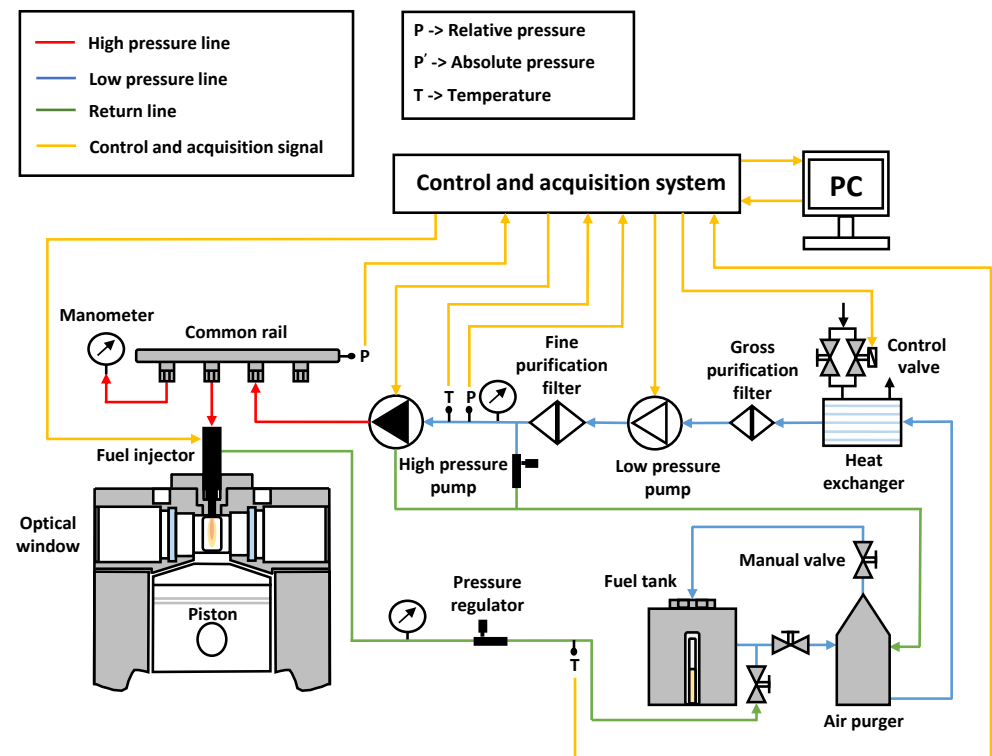

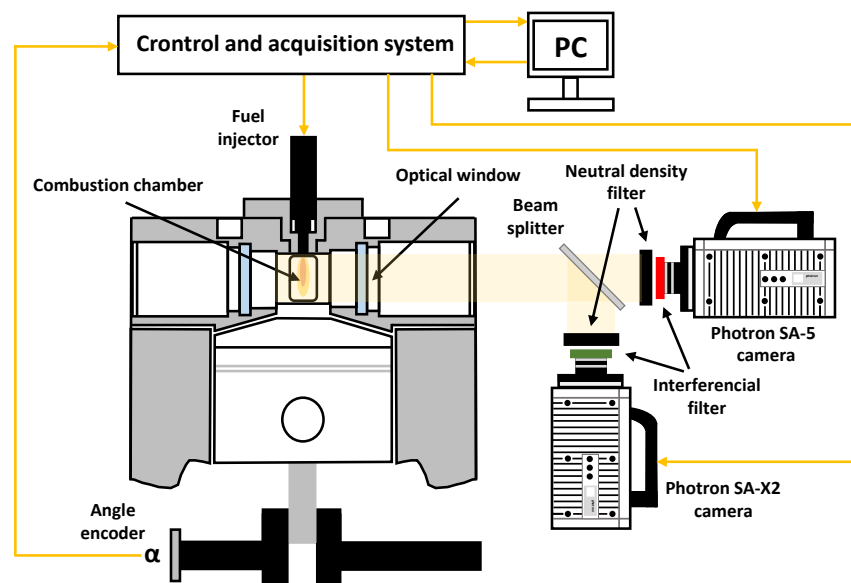**Figure 4.** Scheme of the independent fuel injection system.

Figure 5. Scheme of the two-color pyrometry system used.

To ensure a pixel-by-pixel correspondence between both cameras, they must be placed at the same distance from the beam splitter to ensure similar image sizes. In addition, the same field of view must be ensured for both cameras. However, it is very difficult to ensure a perfect correspondence with the experimental facility. For this reason, a pre-processing transformation routine must be applied to the images of one of the cameras; this includes translation, rotation, and scaling. Before processing each test, a transformation

matrix needs to be calculated. The first step is to flip the green channel images along the vertical axis to orientate them as they are in the red channel. This is necessary because the optical setup forces the green channel camera to register reflected images of the combustion chamber. Then, a scale-invariant feature transform algorithm [52] is applied to obtain a list of the key points (features) of each channel. Both lists are analyzed, and the matching between key points is calculated. If the distance between a feature F1 of the red channel and a feature F2 of the green channel is lower than the distance of F1 to any other feature, the descriptors are matched [52]. With the coordinates of the successfully matched pairs of features, a spatial transformation matrix is calculated that includes translation, rotation, and scaling. The same set of images is used to calculate a transformation matrix per repetition, and, finally, an average transformation matrix is calculated. After this, the flip along the vertical axis, followed by a spatial 2-D transformation, is applied to each of the green channel images based on the average transformation matrix to ensure a pixel-by-pixel match with the corresponding red channel images.

The two-color pyrometry technique assumes that thermal radiation from a flame depends on the temperature, the wavelength, and the amount of soot present in the flame. Soot radiance (I_{soot}) can be expressed as:

$$I_{soot} = \epsilon \cdot I_b \tag{1}$$

where the emissivity (ϵ) can be obtained from the empirical correlation developed by Hottel and Broughton in 1932 [53]:

$$\epsilon(KL, \lambda) = 1 - e^{\frac{-KL_{2C}}{\lambda^\alpha}} \tag{2}$$

where KL_{2C} is the optical thickness calculated from the two-color pyrometry method. The black-body radiation (I_b) can be obtained from Planck's law:

$$I_b(\lambda, T) = \frac{1}{\lambda^5} \cdot \frac{c_1}{e^{\frac{c_2}{\lambda T}} - 1} \tag{3}$$

where c_1 and c_2 are constants; $c_1 = 1.1910439 \times 10^{-16} \frac{\text{Wm}^2}{\text{sr}}$, and $c_2 = 1.4388 \times 10^{-2}$ mK. Zhao and Ladommatos [54] determined that α depends less on wavelength in the visible range than in the infrared. Wavelengths of 450, 550, and 650 nm were chosen for this work so that $\alpha = 1.39$ for most of the fuels [55]. When Equation (1) is applied to the radiation measured at two different wavelengths, an equation system is created where soot KL_{2C} and temperature can be obtained. However, under certain circumstances and at certain pixels, the radiation combinations could provide solutions without physical meaning. For this reason, prior to solving the equation system, a check is performed. The radiation of each channel is used to calculate a corresponding apparent black-body temperature (derived from Equation (3)). If the temperature of the larger wavelength is higher than that of the lower wavelength, it means that emissivity should be higher than 1 for the first channel (which is not possible). In this situation, artificial KL_{2C} and T values are assigned. After applying the resolution algorithm, a classification is carried out, identifying four groups: zone 1 denotes physically correct solutions within a realistic range of KL_{2C} and temperature values; zone 2 indicates that soot emissivity must be greater than 1, i.e., a non-physical solution; zone 3 denotes physically correct solutions with a temperature above an arbitrary value (in this work, 3000 K); zone 4 denotes physically correct solutions with a KL_{2C} factor below an arbitrary minimum limit (in this work, 0.001). This classification of the solution makes it possible to generate what is called a map of the error areas, which reveals which regions of the image provide "unreliable solutions". This is also useful for evaluating the influence of certain setup parameters, as discussed in the following paragraphs.

To transform gray levels into radiance values, calibration curves are obtained using an OSRAM-calibrated tungsten lamp, model WI 17/G; this allows us to obtain the relationship between the spectral radiance values for the two working wavelengths and the digital

levels captured by the acquisition system. The lamp is located at the same distance from the cameras as from the flame in the combustion chamber [56]. The optical assembly simultaneously registers two images of the same combustion event. Using interference filters, it is ensured that the images taken by the cameras are formed only by radiation corresponding to the desired wavelength [56]. The calibration curves obtained for the different channel settings used in this study are summarized in Figure 6. The slope of each curve represents the different sensitivity obtained for each case. The plot on the left corresponds to the dynamic range comparison, while the one on the right represents the interference filter evaluation. For all the cases, a line is fitted to the calibration points (included in the figure). A good agreement is obtained in all cases, which also confirms the linear behavior of the CMOS sensors. Focusing on the plot on the left, for all cases, the use of neutral density filters to reduce the dynamic range provides calibration curves with a lower slope. This means that the detection system is less sensitive to radiation variations than with the high-dynamic-range configuration. When analyzing the interference filter comparison, the trend is not so clear because the blue filter allows the use of a more sensitive acquisition configuration for this channel, but the red one does not. The digital levels of the flame images are then transformed into radiation thanks to the calibration curves obtained in the calibration process.
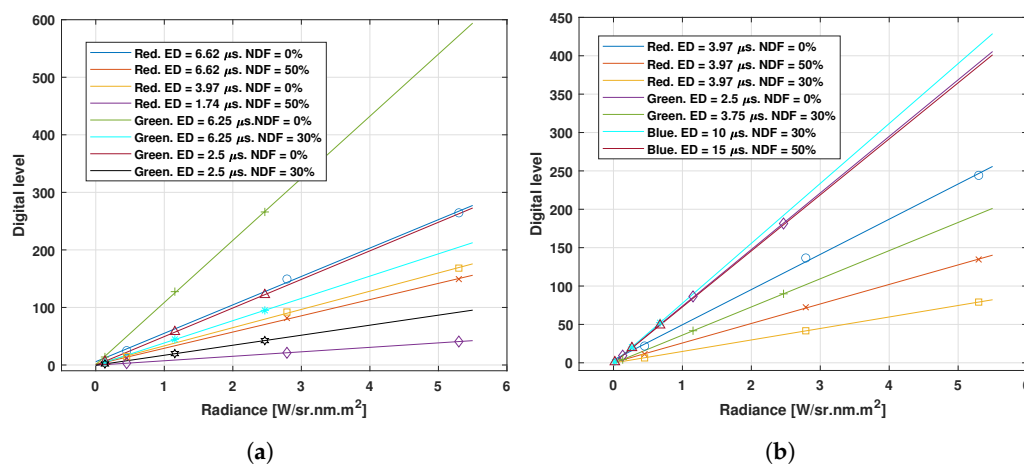

Figure 6. Calibration curves. (**a**) Dynamic range comparison. (**b**) Interference filter comparison.

3. Experimental Procedure

A blend of 30% decane and 70% hexadecane (percentages of mass) was used to perform the tests. A blend of such simple fuels was used because it was expected to form less soot than conventional fuels, thanks to the absence of ring or branched structures, as well as sulfur [57]. Table 2 shows the most relevant properties of the fuel.

Table 2. Fuel properties.

Density at 373 K (kg/m^3)	Derived Cetane Number	C-C Bonds	H/C
703.7	85.4	12.56	2.146

Three operating points corresponding to low, medium, and high soot generation were proposed to determine the influence of the visualization system configuration on soot measurement. Table 3 shows the main characteristics of the operating points.

Table 3. Main characteristics of the operating points.

Operating Points	Energizing Time (µs)	Injection Pressure (bar)	Pressure TDC (bar)	Temperature TDC (K)
Low soot	2000	1500	53	800
Medium soot	2000	1500	53	900
High soot	2000	500	53	900

One of the visualization system characteristics to be evaluated was the use of the dynamic range of the cameras. In this work, this term is used to refer to the portion of the total range of the digital levels of the sensor that are used when registering flame radiation. If similar configuration parameters were used in both detectors, the use of a green or blue filter resulted in images with digital levels close to the minimum sensitivity limit of the sensor. In contrast, the red filter provided digital levels closer to the saturation limit of the detector. When both channels were compared and the two-color pyrometry algorithm was applied, it was observed that the regions where the digital levels in one of the channels were too low (especially when compared to the other) tended to provide non-physical solutions. This may be linked to the influence of different uncertainty sources related to the combustion phenomenon itself (other radiation sources) or the acquisition process [56]. For this reason, this work aimed to characterize the influence of the dynamic range used in both cameras on soot and temperature measurements. For this purpose, four neutral density filters with transmissivity levels of 10, 30, 50, and 70% were used to adjust the dynamic range used by each camera without modifying any other acquisition parameter. Two types of dynamic ranges were defined: high dynamic range, using the higher digital level range of both cameras (no filters used), and low dynamic range (with filter), using the lower detection range.

The second parameter that was evaluated was the influence of the radiation wavelength registered by each camera. The combinations of red (650 nm)–green (550 nm) and red (650 nm)–blue (450 nm) filters were tested. The influence of numerical aperture and exposure duration was also studied, but no notable variations were obtained in the results. Therefore, it was decided not to show these results.

Table 4 shows the test matrix followed to determine the influence of the dynamic range with the red–green filter combination. Table 5 shows the test matrix corresponding to the evaluation of interference filter combinations. Camera settings were defined in an effort to keep the highest possible number of parameters constant between tests. Thus, in both cases, the amount of light registered by each detector was regulated mainly with neutral density filters, without varying exposure duration or lens aperture. For the first study, the lens aperture was kept at f/2.8; for the second study, it was set to f/2. Images were taken on both cameras at a frame rate of 20,000 fps, and the pixel/mm ratio was 8.55. For each test, 10 repetitions were recorded to reduce measurement uncertainties due to cycle-to-cycle variations. Moreover, 30 motored cycles were completed between each combustion cycle to ensure that in-cylinder conditions were not influenced by previous combustion events.

**Table 4.** Dynamic range influence test matrix.

Operating Points	Exposure Duration (Red) (µs)	Neutral Density Filter Opacity (Red) (%)	Exposure Duration (Green) (µs)	Neutral Density Filter Opacity (Green) (%)
Low soot	6.62	0	6.25	0
Low soot	6.62	50	6.25	30
Medium soot	3.97	0	2.5	0
Medium soot	1.74	50	2.5	30
High soot	3.97	0	2.5	0
High soot	1.74	50	2.5	30

Table 5. Interference filter influence test matrix.

| Combination Filters	Operating Points	Exposure Duration (Red) (µs)	Neutral Density Filter Opacity (Red) (%)	Exposure Duration (µs)	Neutral Density Filter Opacity (%)
Red–Green	Low soot	3.97	0	2.5	0
	Medium soot	3.97	50	3.75	30
	High soot	3.97	50	3.75	30
Red–Blue	Low soot	3.97	30	10	30
	Medium soot	3.97	30	15	50
	High soot	3.97	30	15	50

4. Results and Discussion

A set of radiation images from a single combustion cycle is shown in Figure 7. They correspond to a test carried out with the combination of red–green interference filters at the high-soot operating point and high dynamic range. The images above correspond to the red filter, while the images below to the green filter.

| (a) | (b) | (c) | (d) | (e) | (f) |
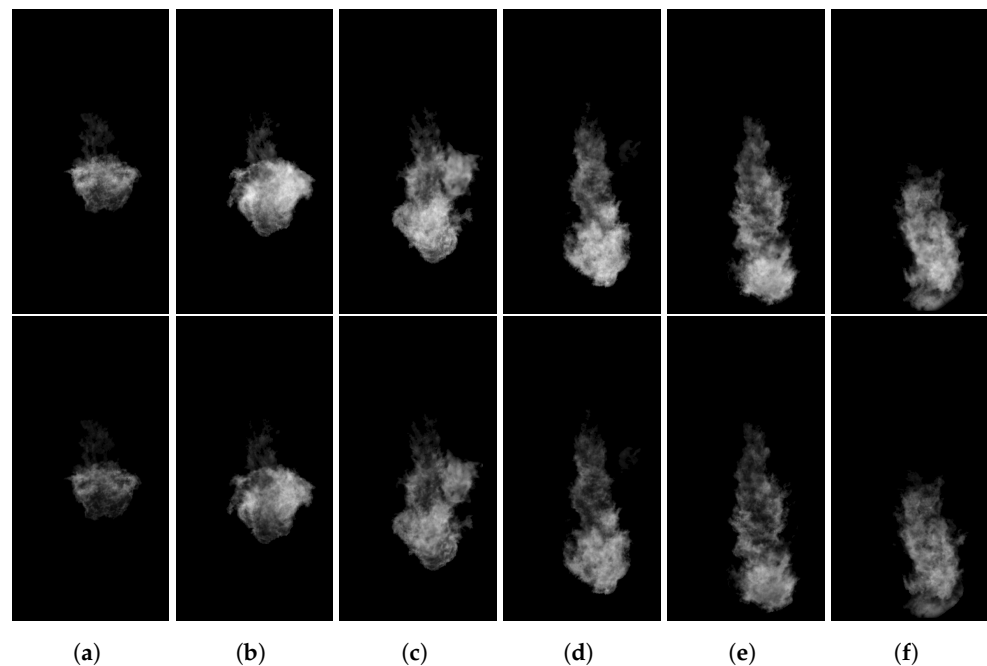
Figure 7. Images corresponding to a test performed with two-color pyrometry. Images were captured in high soot operating conditions and high dynamic range. The images above correspond to the red filter, while those below correspond to the green filter. (**a**) 1500 µs. (**b**) 1850 µs. (**c**) 2200 µs. (**d**) 2550 µs. (**e**) 2900 µs. (**f**) 3250 µs.

Applying Equation (1) pixel-by-pixel to the radiation measured by each camera, the value of KL_{2C} and the temperature are obtained, allowing the construction of a two-dimensional map of these two variables. Figures 8 and 9 show the KL_{2C} and T maps obtained after processing the images in Figure 7. In addition, based on the solution classification described in the previous section, a probability map can be calculated per recorded instant that represents the probability of each pixel to be classified according to the zones previously described. Zone 2 probability maps are shown in the figures that follow. For each recorded instant and pixel, the probability represents the ratio between the number of repetitions where that pixel was classified as zone 2 and the total number of repetitions (10 in this work). The probability maps corresponding to the operating conditions of the images presented in Figure 7 are shown in Figure 10. It can be observed that the regions with greater differences in digital levels between the two channels had a higher probability of obtaining zone 2
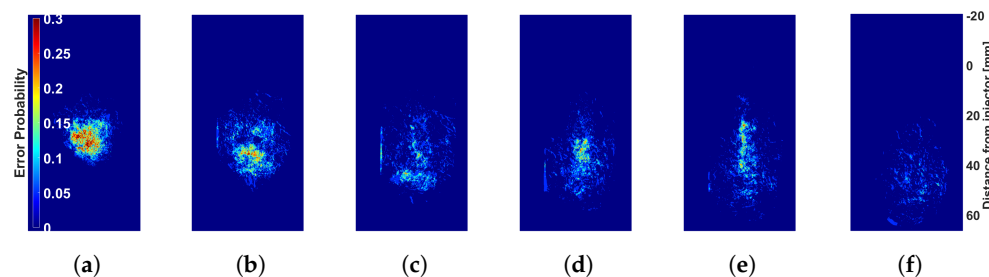
solutions. (See Figures 7 and 10). This demonstrates the importance of controlling the dynamic range of both cameras to obtain more accurate solutions.
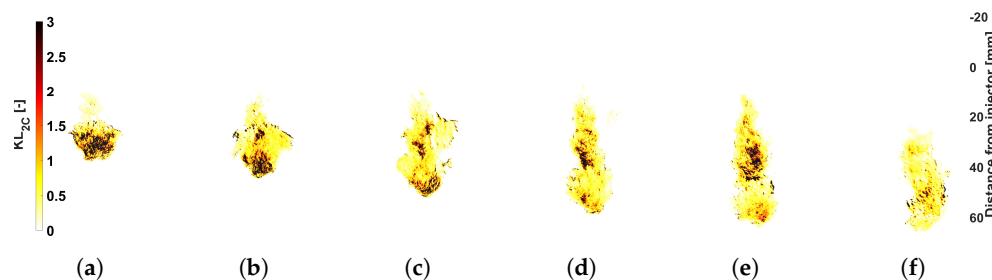
Figure 8. KL_{2C} maps obtained after processing. (**a**) 1500 μs. (**b**) 1850 μs. (**c**) 2200 μs. (**d**) 2550 μs. (**e**) 2900 μs. (**f**) 3250 μs.

Figure 9. T maps obtained after processing. (**a**) 1500 μs. (**b**) 1850 μs. (**c**) 2200 μs. (**d**) 2550 μs. (**e**) 2900 μs. (**f**) 3250 μs.


Figure 10. Error zone probability maps for non-physical solutions after processing. (**a**) 1500 μs. (**b**) 1850 μs. (**c**) 2200 μs. (**d**) 2550 μs. (**e**) 2900 μs. (**f**) 3250 μs.

The dynamic range study was performed for both the red–green and red–blue filter combinations. However, in the following paragraphs, only the results corresponding to the first set of filters are shown because the conclusions obtained with the second set were similar. In addition, for the sake of the clarity of the figures, only the results corresponding to the high- and low-soot operating points are presented because the intermediate point behaved in the same way. Likewise, in order to present information more representative of the process and avoid the influence of cycle-to-cycle engine fluctuations, the soot concentration and the temperature presented from this point on correspond to the averaged values of the 10 repetitions at 2900 μs after the start of energizing (SOE), when the flame is completely developed. In addition, only data obtained along the flame axis are shown to facilitate comparisons between different cases. It is important to highlight that results classified as zone 2 were excluded from the calculations.

Figure 11 shows how the values of KL_{2C} and T varied along the flame axis for the low- and high-dynamic-range conditions and the high- and low-soot operating points. The 95% confidence interval is represented as colored areas around the average curves. It can be observed that the high-dynamic-range setting provided lower KL_{2C} values, especially upstream 45 mm, which was common for both operating points. However, it can also be observed that the temperature values were very similar for both configurations at both operating points. In general, the differences observed between the two configurations were

within the range of the confidence interval represented. Only for high-soot conditions did the region close to the flame tip (around 50 mm) show differences between the two configurations that are out of the confidence interval. Figure 12 shows the error zone probability map for non-physical solutions of the low- and high-dynamic-range test conditions and the high- and low-soot operating points. It can be observed that the results for high dynamic range yielded a lower probability of zone 2 regions. That means that this configuration provided fewer non-physical results, which resulted in more valid data, improving accuracy and statistical reliability in comparison to the low-dynamic-range configuration. In fact, a correspondence can be observed between regions with high zone 2 probability and a larger confidence interval due to fewer data being available. This also suggests that results obtained with the high-dynamic-range configuration are more reliable than the ones corresponding to the other configuration.
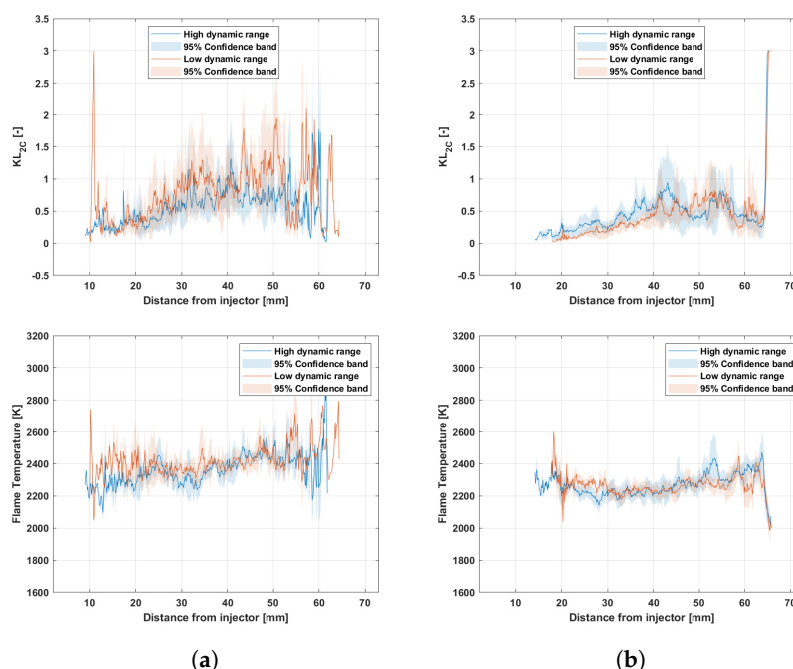

Figure 11. Comparison of high and low dynamic range for KL_{2C} and temperature. t = 2900 µs. (**a**) High soot. (**b**) Low soot.

Finally, the results obtained with both combinations of interference filters are presented to determine their influence. As in the previous results, only the results for the high- and low-soot operating points are presented.

Figure 13 shows how the KL_{2C} and temperature values varied along the flame axis for the two filter combinations and the high- and low-soot operating points. The 95% confidence interval is represented as colored areas around the average values. It is observed that the combination of red–blue filters yielded lower KL_{2C} values for both operating points. On the other hand, it can be seen that the combination of red–blue filters yielded slightly higher temperature values at both operating points. In general, the differences were within the range of the confidence interval. However, for the low-soot case, large differences between 40 and 60 mm can be observed for both KL_{2C} and T (even larger than the corresponding confidence interval). Figure 14 shows the error zone probability map for the non-physical solutions of the two filter combinations and the high- and low-soot operating points. It is observed that the combination of red–green filters generated more zone 2 errors in the area between 40 and 60 mm, where major differences were recorded. Therefore, it can be stated that the results shown in Figure 13 are more reliable for the red–blue combination than for the red–green
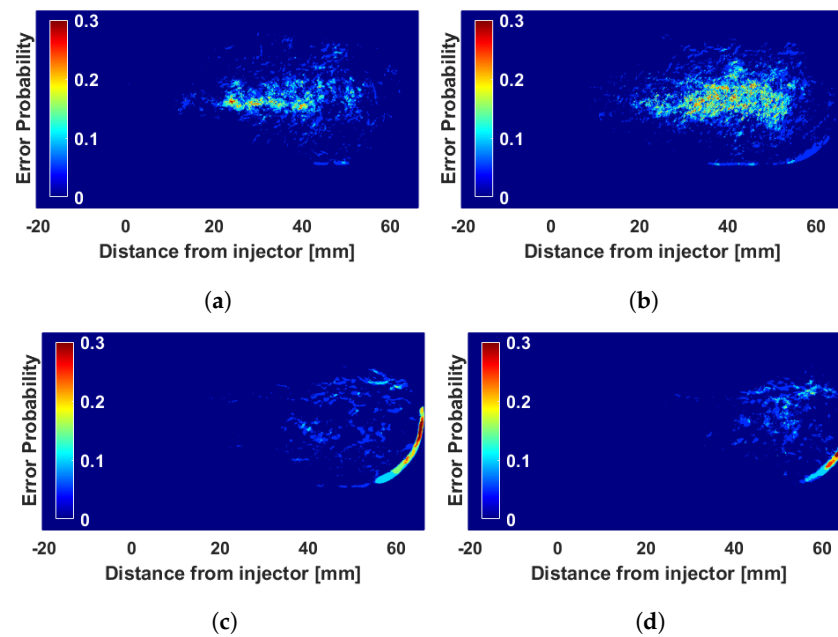
Figure 12. Error zone probability maps for non-physical solutions. t = 2900 μs. (**a**) High dynamic range and high soot; (**b**) low dynamic range and high soot; (**c**) high dynamic range and low soot; (**d**) low dynamic range and low soot.
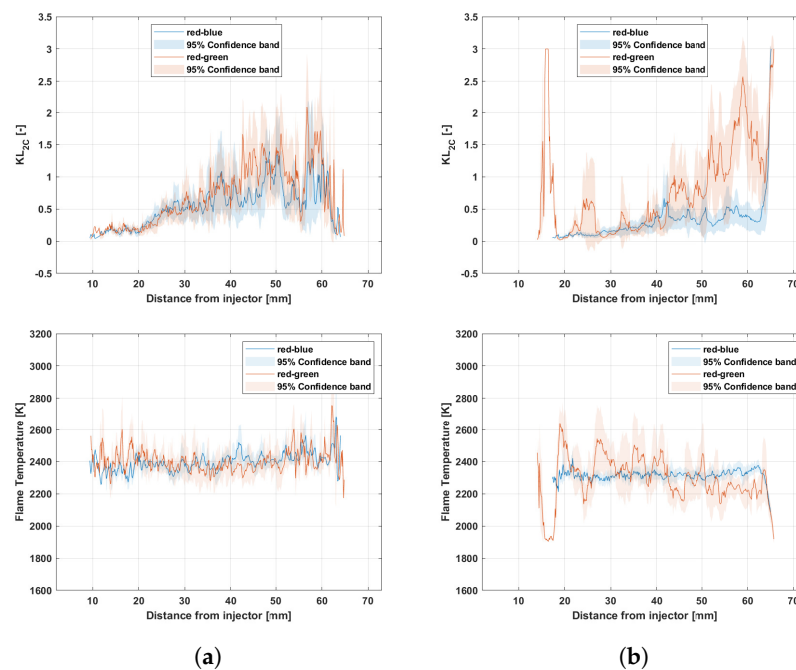
Figure 13. Comparison of KL_{2C} and temperature values for the two filter combinations. t = 2900 μs. (**a**) High soot. (**b**) Low soot.
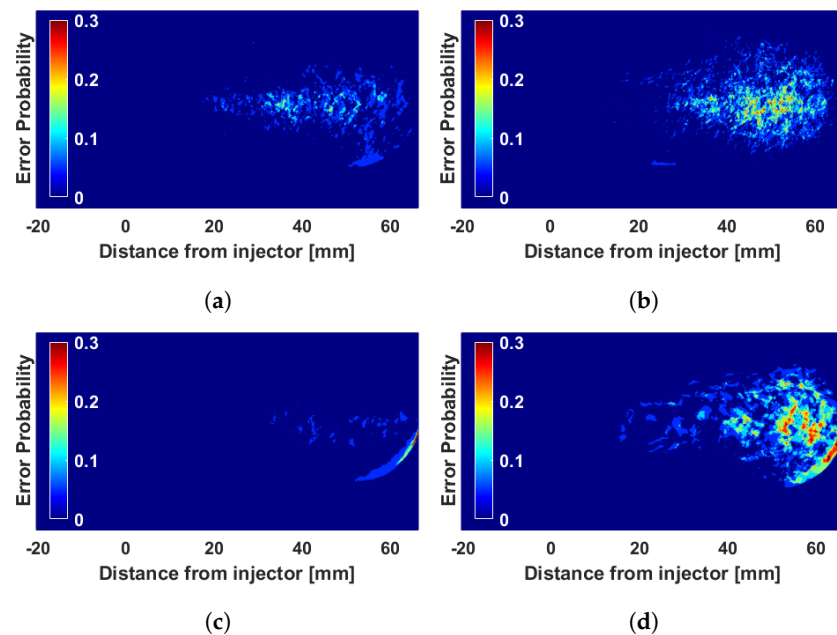
Figure 14. Error zone probability maps for non-physical solutions. t = 2900 μs. (**a**) Red–blue filters and high soot; (**b**) red–green filters and high soot; (**c**) red–blue filters and low soot; (**d**) red–green filters and low soot.

The high-soot operating point is reached by increasing the cylinder temperature and reducing the injection pressure. This produces a flame with more soot (more KL) and higher temperature. In the results, it can be seen that all the configurations evaluated are capable of characterizing this increase compared to the low-soot case (Figures 11 and 13). However, for the combination of red–green filters and the configuration used in the study of interferential filters for low-soot conditions, the KL difference is not so clear. In this case, the exposure times were lower than those used in the dynamic range study for that pair of filters, which probably caused the green-filter camera to work closer to the sensitivity threshold. This resulted in a higher probability of error at the tip of the flame, as can be seen by comparing Figures 12d and 14d. This represents a greater uncertainty of the measurement that, in this case, affects the precision of the results, as can be seen in Figure 13b for the case of KL with the red–green filters. This greater uncertainty in the measurement is also reflected in the temperature, which shows a large oscillation and a lower temperature value in the frontal zone of the flame.

5. Conclusions

This work describes an experimental installation for the investigation of the combustion and injection processes. Optical access allows the study of the processes of injection, atomization, and evaporation of the fuel jet in an inert atmosphere (nitrogen) and the combustion process in a reactive atmosphere (ambient air). In this work, a two-color pyrometry technique was used to study the influence of dynamic range and optical assembly interference filters on the measurement of soot under reaction conditions inside the cylinder.

Regarding the tests carried out with two-color pyrometry, firstly, the images obtained in the tests and their subsequent processing to obtain maps of KL_{2C}, temperature, and error probability are presented herein. Subsequently, the results for the combination of red–green interference filters are shown to determine how dynamic range affects the measurement of soot formation within the flame. Finally, the comparative study between two combinations of interference filters is presented to determine the influence on soot measurement. After analyzing the results obtained, it can be concluded that:

- Working with cameras in high dynamic range (no filter) provides better results since the system seems to be less sensitive to measurement noise, and fewer points with a non-physical solution are obtained. This is seen for the three operating points studied in this work. Despite the differences, it seems that the different configurations used are capable of determining the combustion behavior according to the changes in the operating conditions used in this work.
- The combination of red–blue interference filters provides better results, yielding a much smaller area of non-physical solutions. This is because the greater the difference between the wavelengths of the two interference filters, the fewer points there are with non-physical solutions. For low-soot conditions, significant discrepancies were seen, including values that did not represent the differences in operating conditions or the effect they should have on combustion.

Summarizing these two previous points, it can be stated that better results are obtained working with cameras in high dynamic range (no filter) with a combination of red–blue interference filters. On the other hand, in future works, this technique will be compared with the diffused back-illumination extinction (DBI) technique. To apply this technique, two aligned optical access points are necessary. The installation described here does possess this feature; however, in general, it is practically impossible in more common optical engines with more limited optical access.

References

1. Birol, F. *World Energy Outlook*; International Energy Agency: Paris, France, 2010; Volume 1.
2. Khatib, H. IEA world energy outlook 2011—A comment. *Energy Policy* **2012**, *48*, 737–743. [CrossRef]
3. Nabi, M.N.; Rahman, M.M.; Akhter, M.S. Biodiesel from cotton seed oil and its effect on engine performance and exhaust emissions. *Appl. Therm. Eng.* **2009**, *29*, 2265–2270. [CrossRef]
4. ConairSystem. New Diesel Engine for UAV and GA. Available online: http://www.conairsystem.com/en/projects/new-diesel-engine.html (accessed on 15 June 2022).
5. Cosworth. Aerospace Unmanned Aerial Vehicle (UAV). Available online: https://www.cosworth.com/capabilities/electrification/motor/aerospace-uav/ (accessed on 15 June 2022).
6. Borchardt, J.K. Unmanned aerial vehicles spur composites use. *Reinf. Plast.* **2004**, *48*, 28–31. [CrossRef]
7. Finn, R.L.; Wright, D. Unmanned aircraft systems: Surveillance, ethics and privacy in civil applications. *Comput. Law Secur. Rev.* **2012**, *28*, 184–194. [CrossRef]
8. Dudek, M.; Tomczyk, P.; Wygonik, P.; Korkosz, M.; Bogusz, P.; Lis, B. Hybrid fuel cell–battery system as a main power unit for small unmanned aerial vehicles (UAV). *Int. J. Electrochem. Sci.* **2013**, *8*, 8442–8463.
9. Thibbotuwawa, A.; Nielsen, P.; Zbigniew, B.; Bocewicz, G. Energy consumption in unmanned aerial vehicles: A review of energy consumption models and their relation to the UAV routing. In Proceedings of the International Conference on Information Systems Architecture and Technology, Wroclaw, Poland, 15–17 September 2018; Springer: Berlin/Heidelberg, Germany, 2018; pp. 173–184.
10. Li, J.; Zhou, L.; Zhao, Z.; Wang, X.; Zhang, F. Research on knocking characteristics of kerosene spark-ignition engine for unmanned aerial vehicle (UAV) by numerical simulation. *Therm. Sci. Eng. Prog.* **2019**, *9*, 1–10. [CrossRef]

11. Lee, J.; Bae, C. Application of JP-8 in a heavy duty diesel engine. *Fuel* **2011**, *90*, 1762–1770. [CrossRef]

12. Korres, D.M.; Karonis, D.; Lois, E.; Linck, M.B.; Gupta, A.K. Aviation fuel JP-5 and biodiesel on a diesel engine. *Fuel* **2008**, *87*, 70–78. [CrossRef]

13. Baird, B.; Etemad, S. *Advanced Glow Plug for Heavy Fuels Applications*; SAE Technical Paper; SAE: Warrendale, PA, USA, 2013.

14. Ning, L.; Duan, Q.; Wei, Y.; Zhang, X.; Yang, B.; Zeng, K. Experimental investigation on combustion and emissions of a two-stroke DISI engine fueled with aviation kerosene at various compression ratios. *Fuel* **2020**, *259*, 116–224. [CrossRef]

15. Duddy, B.J.; Lee, J.; Walluk, M.; Hallbach, D. Conversion of a spark-ignited aircraft engine to JP-8 heavy fuel for use in unmanned aerial vehicles. *SAE Int. J. Engines* **2011**, *4*, 82–93. [CrossRef]

16. Hooper, P. Initial development of a multi-fuel stepped piston engine for unmanned aircraft application. *Aircr. Eng. Aerosp. Technol.* **2001**, *73*, 459–465. [CrossRef]

17. Dinc, A.; Otkur, M. Emissions prediction of an aero-piston gasoline engine during surveillance flight of an unmanned aerial vehicle. *Aircr. Eng. Aerosp. Technol.* **2020**, *93*, 462–472. [CrossRef]

18. Mangus, M.; Depcik, C. Comparison of ULSD, used cooking oil biodiesel, and JP-8 performance and emissions in a single-cylinder compression-ignition engine. *SAE Int. J. Fuels Lubr.* **2012**, *5*, 1382–1394. [CrossRef]

19. Arkoudeas, P.; Kalligeros, S.; Zannikos, F.; Anastopoulos, G.; Karonis, D.; Korres, D.; Lois, E. Study of using JP-8 aviation fuel and biodiesel in CI engines. *Energy Convers. Manag.* **2003**, *44*, 1013–1025. [CrossRef]

20. Fernandes, G.; Fuschetto, J.; Filipi, Z.; Assanis, D.; McKee, H. Impact of military JP-8 fuel on heavy-duty diesel engine performance and emissions. *Proc. Inst. Mech. Eng. Part D J. Automob. Eng.* **2007**, *221*, 957–970. [CrossRef]

21. Gowdagiri, S.; Cesari, X.M.; Huang, M.; Oehlschlaeger, M.A. A diesel engine study of conventional and alternative diesel and jet fuels: Ignition and emissions characteristics. *Fuel* **2014**, *136*, 253–260. [CrossRef]

22. Corral-Gómez, L.; Rubio-Gómez, G.; Martínez-Martínez, S.; Sánchez-Cruz, F. Effect of diesel-biodiesel-ethanol blends on the spray macroscopic parameters in a common-rail diesel injection system. *Fuel* **2019**, *241*, 876–883. [CrossRef]

23. EASA. Implementation of the Latest CAEP Amendmentsto ICAO Annex 16 Volumes I, II and III. 2019. Available online: https://www.easa.europa.eu/sites/default/files/dfu/NPA%202020-06.pdf (accessed on 15 June 2022).

24. Neves, R.C.; Klein, B.C.; da Silva, R.J.; Rezende, M.C.A.F.; Funke, A.; Olivarez-Gómez, E.; Bonomi, A.; Maciel-Filho, R. A vision on biomass-to-liquids (BTL) thermochemical routes in integrated sugarcane biorefineries for biojet fuel production. *Renew. Sustain. Energy Rev.* **2020**, *119*, 109607. [CrossRef]

25. Flynn, P.; Mizusawa, M.; Uyehara, O.A.; Myers, P.S. An experimental determination of the instantaneous potential radiant heat transfer within an operating Diesel engine. *SAE Trans.* **1972**, *81*, 95–126.

26. Boulouchos, K.; Eberle, M.; Ineichen, B.; Klukowski, C. New insights into the mechanisms of in-cylinder heat transfer in diesel engines. *SAE Trans.* **1989**, *98*, 1064–1082.

27. Kim, T.; Alder, B.; Laurendeau, N.; Gore, J. Effects of partial premixing on NO_x emission indices of soot-containing flames. *Combust. Sci. Tech.* **1995**, *111*, 361–370. [CrossRef]

28. Akihama, K.; Takatori, Y.; Inagaki, K.; Sasaki, S.; Dean, A.M. Mechanism of the smokeless rich diesel combustion by reducing temperature. *SAE Trans.* **2001**, *110*, 648–662.

29. Ogawa, H.; Li, T.; Miyamoto, N. Characteristics of low temperature and low oxygen diesel combustion with ultra-high exhaust gas recirculation. *Int. J. Engine Res.* **2007**, *8*, 365–378. [CrossRef]

30. Xuan, T.; Pastor, J.V.; García-Oliver, J.M.; García, A.; He, Z.; Wang, Q.; Reyes, M. In-flame soot quantification of diesel sprays under sooting/non-sooting critical conditions in an optical engine. *Appl. Therm. Eng.* **2019**, *149*, 1–10. [CrossRef]

31. Baert, R.S.; Frijters, P.J.; Somers, B.; Luijten, C.C.; de Boer, W. *Design and Operation of a High Pressure, High Temperature Cell for HD Diesel Spray Diagnostics: Guidelines and Results*; SAE Technical Paper; SAE: Warrendale, PA, USA, 2009.

32. Parker, A.; Wanstall, C.T.; Reggeti, S.A.; Bittle, J.A.; Agrawal, A.K. Simultaneous rainbow schlieren deflectometry and OH* chemiluminescence imaging of a diesel spray flame in constant pressure flow rig. *Proc. Combust. Inst.* **2020**, *38*, 5557–5565. [CrossRef]

33. Yip, H.; Fattah, I.R.; Yuen, A.; Yang, W.; Medwell, P.; Kook, S.; Yeoh, G.; Chan, Q. Flame–wall interaction effects on diesel post-injection combustion and soot formation processes. *Energy Fuels* **2019**, *33*, 7759–7769. [CrossRef]

34. Fattah, I.R.; Ming, C.; Chan, Q.; Wehrfritz, A.; Pham, P.; Yang, W.; Kook, S.; Medwell, P.; Yeoh, G.; Hawkes, E.; et al. Spray and combustion investigation of post injections under low-temperature combustion conditions with biodiesel. *Energy Fuels* **2018**, *32*, 8727–8742. [CrossRef]

35. Payri, R.; Gimeno, J.; Viera, J.P.; Plazas, A.H. Needle lift profile influence on the vapor phase penetration for a prototype diesel direct acting piezoelectric injector. *Fuel* **2013**, *113*, 257–265. [CrossRef]

36. Payri, R.; Salvador, F.J.; Martí-Aldaraví, P.; Vaquerizo, D. ECN Spray G external spray visualization and spray collapse description through penetration and morphology analysis. *Appl. Therm. Eng.* **2017**, *112*, 304–316. [CrossRef]

37. Bermúdez, V.; García, J.; Juliá, E.; Martínez, S. *Engine with Optically Accessible Cylinder Head: A Research Tool for Injection and Combustion Processes*; SAE Technical Paper; SAE: Warrendale, PA, USA, 2003.

38. Mancaruso, E.; Merola, S.; Vaglieco, B. Study of the multi-injection combustion process in a transparent direct injection common rail diesel engine by means of optical techniques. *Int. J. Engine Res.* **2008**, *9*, 483–498. [CrossRef]

39. Pastor, J.; Payri, R.; Gimeno, J.; Nerva, J. Experimental study on RME blends: Liquid-phase fuel penetration, chemiluminescence, and soot luminosity in diesel-like conditions. *Energy Fuels* **2009**, *23*, 5899–5915. [CrossRef]

40. Fang, T.; Lin, Y.C.; Foong, T.M.; Lee, C.f. Biodiesel combustion in an optical HSDI diesel engine under low load premixed combustion conditions. *Fuel* **2009**, *88*, 2154–2162. [CrossRef]

41. Payri, R.; Gimeno, J.; Bardi, M.; Plazas, A.H. Study liquid length penetration results obtained with a direct acting piezo electric injector. *Appl. Energy* **2013**, *106*, 152–162. [CrossRef]

42. Payri, R.; Salvador, F.; Garcia, A.; Gil, A. Combination of visualization techniques for the analysis of evaporating diesel sprays. *Energy Fuels* **2012**, *26*, 5481–5490. [CrossRef]

43. Briceño Sánchez, F.J. Aportaciones al Estudio de la Evolución Transitoria de Llamas de Difusión Diesel. Ph.D. Thesis, Universitat Politècnica de València, Valencia, Spain, 2016.

44. Xuan, T. Optical Investigations on Diesel Spray Dynamics and in-Flame Soot Formation. Ph.D. Thesis, Universitat Politècnica de València, Valencia, Spain, 2018.

45. Yon, J.; Cruz, J.J.; Escudero, F.; Morán, J.; Liu, F.; Fuentes, A. Revealing soot maturity based on multi-wavelength absorption/emission measurements in laminar axisymmetric coflow ethylene diffusion flames. *Combust. Flame* **2021**, *227*, 147–161. [CrossRef]

46. Densmore, J.M.; Biss, M.M.; McNesby, K.L.; Homan, B.E. High-speed digital color imaging pyrometry. *Appl. Opt.* **2011**, *50*, 2659–2665. [CrossRef]

47. Pastor, J.V.; García, A.; Micó, C.; Lewiski, F. Simultaneous high-speed spectroscopy and 2-color pyrometry analysis in an optical compression ignition engine fueled with OMEX-diesel blends. *Combust. Flame* **2021**, *230*, 111437. [CrossRef]

48. Pastor, J.V.; García, A.; Micó, C.; Lewiski, F. An optical investigation of Fischer-Tropsch diesel and Oxymethylene dimethyl ether impact on combustion process for CI engines. *Appl. Energy* **2020**, *260*, 114238. [CrossRef]

49. Zhang, J.; Jing, W.; Roberts, W.L.; Fang, T. Soot temperature and KL factor for biodiesel and diesel spray combustion in a constant volume combustion chamber. *Appl. Energy* **2013**, *107*, 52–65. [CrossRef]

50. Jeon, J.; Park, S. Effect of injection pressure on soot formation/oxidation characteristics using a two-color photometric method in a compression-ignition engine fueled with biodiesel blend (B20). *Appl. Therm. Eng.* **2018**, *131*, 284–294. [CrossRef]

51. Fu, T.; Liu, J.; Tian, J. VIS-NIR multispectral synchronous imaging pyrometer for high-temperature measurements. *Rev. Sci. Instrum.* **2017**, *88*, 064902. [CrossRef] [PubMed]

52. Lowe, D.G. Distinctive image features from scale-invariant keypoints. *Int. J. Comput. Vis.* **2004**, *60*, 91–110. [CrossRef]

53. Hottel, H.C.; Broughton, F. Determination of true temperature and total radiation from luminous gas flames. *Ind. Eng. Chem. Anal. Ed.* **1932**, *4*, 166–175. [CrossRef]

54. Zhao, H.; Ladommatos, N. Optical diagnostics for soot and temperature measurement in diesel engines. *Prog. Energy Combust. Sci.* **1998**, *24*, 221–255. [CrossRef]

55. Zhao, H.; Ladommatos, N. *Engine Combustion Instrumentation and Diagnostics*; Society of Automotive Engineers: Warrendale, PA, USA, 2001.

56. Payri, F.; Pastor, J.V.; García, J.; Pastor, J.M. Contribution to the application of two-colour imaging to diesel combustion. *Meas. Sci. Technol.* **2007**, *18*, 2579. [CrossRef]

57. Tree, D.R.; Svensson, K.I. Soot processes in compression ignition engines. *Prog. Energy Combust. Sci.* **2007**, *33*, 272–309. [CrossRef]